ADVANCED MATERIALS INTERFACES
www.advmatinterfaces.de

Structural and Trap-State Density Enhancement in Flash Infrared Annealed Perovskite Layers

*Alica Brunova, Karol Vegso, Vojtech Nadazdy, Peter Nadazdy, Riyas Subair, Matej Jergel, Eva Majkova, Pallavi Pandit, Stephan V. Roth, Alexander Krasnansky, Alexander Hinderhofer, Frank Schreiber, Jianjun Tian, and Peter Siffalovic**

Perovskite solar cells are well-known for their high energy conversion efficiency, low-temperature processing, and cost-effective production. Flash infrared annealing (FIRA) of slot-die cast perovskite precursors offers an attractive manufacturing route using high-throughput roll-to-roll technology. Despite the recent progress in FIRA perovskite annealing, the optimal composition of the perovskite precursor is yet to be developed. Here, the effect of methylammonium chloride (MACl) on the perovskite structure and trap-state density as a function of the FIRA annealing time is investigated. In situ real-time grazing-incidence wide-angle X-ray scattering (GIWAXS) is employed to monitor the perovskite layer formation during FIRA annealing with millisecond temporal resolution. In addition, the density of states in the bandgap is estimated using ex situ energy-resolved electrochemical impedance spectroscopy. Evidence is found that adding 10% MACl into the perovskite precursor solution significantly improves the crystallographic orientation of the perovskite layers while reducing the trap-state density by one order of magnitude. In addition, using time-resolved GIWAXS, the most favorable time window for the FIRA processing of perovskite films with the lowest mosaicity and trap-state density is identified. The results are of general importance for elucidating the appropriate temporal windows in complex and fast-evolving crystallization processes.

1. Introduction

More than a decade ago, Kojima et al.[1] demonstrated that organic–inorganic lead halide perovskite compounds can be employed as visible-light sensitizers in conventional dye-sensitized solar cells. The most studied perovskite compound is methylammonium lead iodide ($CH_3NH_3PbI_3$, MAPI), although it is not moisture resistant and may be hazardous to the environment. Lee et al.[2] showed that perovskite thin layers could be used directly for harvesting solar radiation similar to inorganic semiconductors. Since then, tremendous advances have been made in optimizing perovskite solar cells (PSCs), with power conversion efficiencies (PCE) reaching 25.5% and thus coming to the proximity of single-crystal Si solar cells with a record PCE of 26.1%.

The initial difficulties in preparing homogeneous perovskite films were overcome by introducing an antisolvent technique,[3,4] in which a small amount of a nonpolar solvent is used to induce heterogeneous nucleation of perovskite films. However, the antisolvent technique is not suitable for upscaling as it relies on spin-coating technology. Hence, a large number of different deposition techniques[5,6] were developed to cast perovskite thin films using scalable technologies such as spray coating, inkjet printing, slot-die coating, blade coating, vacuum thermal evaporation, etc.

Another way to improve the film homogeneity and crystallinity is to induce the formation of crystalline colloidal clusters

A. Brunova, Dr. K. Vegso, Dr. V. Nadazdy, Dr. P. Nadazdy, Dr. R. Subair, Dr. M. Jergel, Dr. E. Majkova, Dr. P. Siffalovic
Institute of Physics
Slovak Academy of Sciences
Dúbravská cesta 9, Bratislava 845 11, Slovakia
E-mail: peter.siffalovic@savba.sk

Dr. K. Vegso, Dr. V. Nadazdy, Dr. M. Jergel, Dr. E. Majkova, Dr. P. Siffalovic
Centre for Advanced Materials Application
Slovak Academy of Sciences
Dúbravská cesta 9, Bratislava 845 11, Slovakia

Dr. P. Pandit, Prof. S. V. Roth
Photon Science
Deutsches Elektronen-Synchrotron (DESY)
22607 Hamburg, Germany

The ORCID identification number(s) for the author(s) of this article can be found under https://doi.org/10.1002/admi.202100355.

Prof. S. V. Roth
KTH Royal Institute of Technology
Department of Fibre and Polymer Technology
Teknikringen 56-58, Stockholm SE-100 44, Sweden

A. Krasnansky
Department of Physics
Boston University
233 Bay State Road, Boston, MA 02215, USA

Dr. A. Hinderhofer, Prof. F. Schreiber
Institute of Applied Physics
University of Tübingen
Auf der Morgenstelle 10, D-72076 Tübingen, Germany

Prof. J. Tian
Institute for Advanced Materials and Technology
University of Science and Technology Beijing
Beijing 100083, China

DOI: 10.1002/admi.202100355

in the perovskite precursor solution,[7] which serve as seed crystals for the nucleation of perovskite film. Among other chemical additives, methylammonium chloride (MACl) was found to be effective in the coordination between the components of the precursor solution.[8–12] The MACl can coordinate with dimethylformamide (DMF), methylammonium iodide (MAI), and PbI_2 to form a complex that has a larger size than the complex in the standard precursor solution without MACl. This has a direct effect on the grain size distribution in the final perovskite films. As a result, improved optoelectronic performance was observed in the MACl-assisted perovskite solar cells, mainly due to fewer grain boundaries that negatively influence charge transport.

To induce controlled perovskite crystallization, flash infrared annealing (FIRA) was recently introduced[13–18] as a highly efficient technique enabling quick manufacturing of highly efficient and stable PSCs. Here, a short pulse of intense infrared radiation is employed to induce nucleation and growth of perovskite crystals in thin films. The FIRA method enables crystallization of perovskite films within a few seconds, which is mandatory for large-scale roll-to-roll production on flexible substrates.

An important aspect of perovskite film preparation is the growth of films with crystallographically well-aligned large perovskite grains with the least possible number of grain boundaries, which mimic conventional semiconductor solar cells based on monocrystalline materials.[19,20] In general, the grain boundaries and the interfaces of perovskites to the hole- and electron-conducting layers are possible recombination centers for charge carriers. In ideal solar cells that reach the Shockley–Queisser limit, radiative recombination is the only allowed recombination process.[21,22] Notwithstanding the controversy over the importance of the crystal orientation and grain size[23] for the optoelectronic properties of PSCs, the majority of the theoretical and experimental works identified the grain boundaries and layer interfaces as the principal sources of the subgap electronic states that facilitate recombination.[24–34] Despite the remarkably defect tolerance of perovskite materials,[35–37] the development of manufacturing techniques that reduce the trap-state densities in the bandgap is critical.

State-of-the-art crystallographic investigations during the formation of perovskite thin films are based on time-resolved in situ grazing-incidence X-ray scattering techniques.[38] Employing synchrotron radiation, a large number of studies on the crystallization pathways of perovskite films were published.[39–57] Structural changes, particularly defects, alter the electronic structure and induce the generation of trap states in bandgap that increase the nonradiative recombination rate, which adversely affects the PCE of PSCs.

The present study focuses on the correlation between the crystallographic structure and trap-state density of perovskite films prepared by FIRA as a function of different amounts of MACl additive. For ex situ structural studies, we used laboratory-based grazing-incidence wide-angle X-ray scattering (GIWAXS). We found that 10 mol% of MACl additive significantly improved the crystallographic orientation of the perovskite films. The FIRA annealing leads to the formation of perovskite grains with uniaxial texture. In addition, real-time and in situ GIWAXS studies of perovskite crystallization were carried out using high-brilliant synchrotron radiation, which enabled a millisecond temporal resolution essential for tracking the FIRA annealing process. Using time-resolved GIWAXS studies, we have identified a suitable temporal processing window for the production of perovskite films with the lowest mosaicity and trap-state density.

The trap states facilitate the nonradiative recombination of charge carriers and must therefore be minimized. So far, the density of trap states has been measured using space-charge limited current analysis, deep level transient spectroscopy, and thermal admittance spectroscopy.[58,59] In our study, the influence of perovskite film mosaicity on the density of trap states was investigated using energy-resolved electrochemical impedance spectroscopy (ER-EIS). This method enables the mapping of trap-state density in the bandgap over a wide dynamic range.[60–63] We confirmed a decrease in the trap-state density in the bandgap by one order magnitude for the FIRA-annealed perovskite layers with 10 mol% of MACl additive compared to the layers without MACl additive. Furthermore, we correlated the ongoing structural changes assessed by the time-resolved GIWAXS during the FIRA treatment with the evolution of the trap-state density. The unique combination of time-resolved GIWAXS and trap-state spectroscopy used here enables the identification of appropriate temporal windows for fast crystallization processes in general.

2. Results and Discussion

The addition of MACl additive to the conventional perovskite precursor solution profoundly affects the nucleation and crystallization during FIRA. We utilized ex situ GIWAXS to characterize the changes in the perovskite film mosaicity (preferential crystallographic orientation of the perovskite grains) after annealing by FIRA (10 s) for varying amounts of MACl additive, expressed in molar fractions of MAI. **Figure 1** shows the final GIWAXS patterns of perovskite films with MACl amounts between 0% and 50% after annealing that were taken at room temperature.

We observed no evidence that Cl was incorporated into the perovskite lattice, even at a 50% MACl:MAI ratio in the precursor solution. Instead, we find only one perovskite structure corresponding to the unit cell of pure MAPI. Note that the diffraction peaks were indexed using a_ tetragonal lattice, unlike the time-resolved GIWAXS patterns measured above the phase transition temperature of 54 °C to the cubic phase.[64,65] The perovskite films cast from the precursor solution without MACl additive display a continuous 110/002 diffraction ring at $q \approx 1$ Å^{-1}, since the GIWAXS measurement geometry does not allow to separate the 110 and 002 diffraction peaks spatially. This indicates a random orientation of the perovskite crystals in the final film. On the other hand, all perovskite layers prepared with the MACl additive show a uniaxial texture with the (112) lattice planes parallel to the substrate surface (Figure 1b–f). Detailed information on the unit cell orientation (Figure S2, Supporting Information) of the prepared perovskite films can be found in the Supporting Information. The lowest film mosaicity was found for the 10% MACl molar fraction. When the molar content is increased above 10%, the smearing of 110/002 diffraction spots suggests a deterioration in the mosaicity.

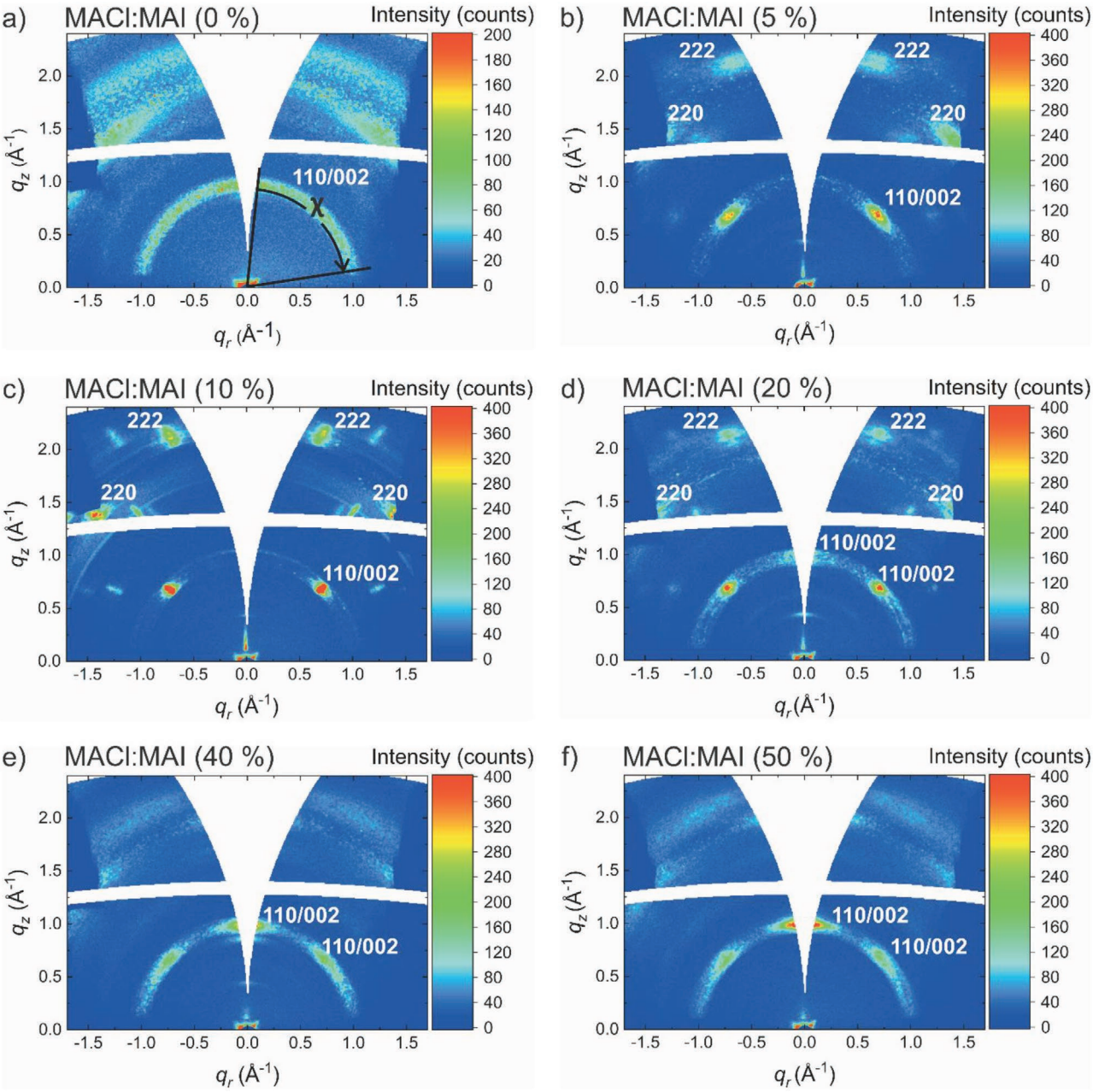

Figure 1. The GIWAXS patterns of perovskite layers after FIRA (10 s) with different amounts of MAI replaced by MACl: a) 0% (without MACl), b) 5%, c) 10%, d) 20%, e) 40%, and f) 50%. The black arrow indicates the integrated azimuthal trace along the χ angle used in Figure 2a.

The perovskite film mosaicity was quantified using so-called χ cuts.[56] To obtain the χ cuts shown in **Figure 2**a, the intensities in GIWAXS patterns (Figure 1) were integrated in a q range () of 0.9–1.1 Å^{-1} and plotted as a function of the azimuthal angle χ ($\chi = 0°$ for $q_r = 0$ as schematically indicated in Figure 1a). The peaks in all χ cuts depicted in Figure 2a are located at the χ value of 45°. Both the area and full width at half maximum (FWHM) of the χ peak reach maximal values for the MACl molar fraction of 10% as shown in Figure 2b. The area under the χ peak is proportional to the volume of the crystalline perovskite phase. By contrast, the width of the χ peak is associated with the angular misalignment of the perovskite crystals, namely their (112) lattice planes from the sample surface. Thus, Figure 2b confirms that the film with the lowest mosaicity was developed for the MACl molar fraction of 10% with the (112) lattice planes' misalignment from the surface of only 3.1° ± 0.1°. The origin of the preferential orientation of conventionally annealed perovskite films with MACl additive was thoroughly reviewed by Odysseas Kosmatos et al.[12]

Based on the fact that the MACl molar fraction of 10% gives the lowest mosaicity, we prepared a series of samples with different annealing times ranging from 0.5 to 10 s. The surface topography of selected perovskite films, measured by atomic

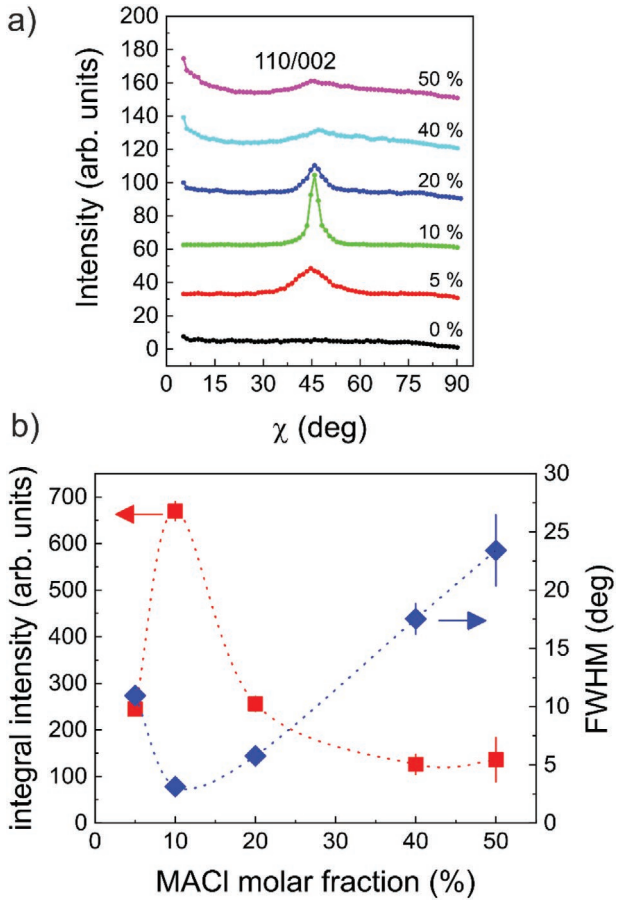

Figure 2. The effect of the MACl additive on the mosaicity of the perovskite layers. a) The azimuthal χ cuts of 110/002 diffractions for different MACl molar fractions. b) The area and FWHM of 110/002 diffraction peaks as a function of the MACl molar fractions. The dotted lines serve as guides to the eye.

force microscopy (AFM) and visible microscopy, is shown in **Figure 3**. After annealing for less than 3 s, the perovskite layer was still wet and drying, forming a needle-like structure with a large number of pinholes (Figure 3a). Such a structure is not suitable for photovoltaic applications.

On the microscale, optical microscopy revealed a homogenous layer (Figure 3e). After 3 s annealing, the perovskite crystallization was not yet complete (Figure 3b,f). AFM confirmed (Figure 3b) the presence of ≈100 µm large clusters of needle-like perovskite grains growing radially from the nucleation sites. A percolated structure of dendrite clusters was formed on the microscale, as confirmed by optical microscopy (Figure 3f). Finally, after 4 s annealing, a continuous layer was obtained. The annealed films were composed of large dendritic clusters in tight contact (Figure 3c). The evaluation of AFM images showed significant height variations across the perovskite grains and can be found in the Supporting Information. On average, the boundary of grain clusters is ≈370 nm lower than the nucleation site located in the central part. This is a well-known limitation of FIRA processing and requires further optimization of the annealing process itself before it can be used to produce PSCs.[23]

So far, we have elucidated the influence of MACl additive on the mosaicity and topography of perovskite films annealed by FIRA. Despite the fact that the size and crystallographic orientation of perovskite grains play an essential role in the performance of PSCs, the influence of the MACl additive on the electronic structure, in particular the density of trap states between the highest occupied molecular orbital (HOMO) and lowest unoccupied molecular orbital (LUMO) states, also needs to be clarified. The trap states located in the bulk and at the surface of MAPI grains, as well as the trap states at the perovskite interfaces with the hole/electron transporting layers, are considered to be the critical recombination centers.[24–34] We employed the ex situ ER-EIS technique to quantify the density of trap states.

We investigated the evolution of density of states (DOS) as a function of FIRA time for the perovskite films cast from the solution with the optimized MACl molar fraction of 10%. The DOS spectra for the perovskite films annealed for 3, 4, 5, and 6 s are shown in **Figure 4**a.

The $g(E)$ scale was calibrated considering the charge-transfer rate constant, $k_{ET} = 2 \times 10^{-24}$ cm^4 s^{-1}. This value was calculated using the relation[66] $k_{ET} = L\omega_{meas}[A]^{-1}$ with the perovskite layer thickness $L = 400$ nm, $\omega_{meas} = 3$ Hz, and $[A] = 6 \times 10^{19}$ cm^{-3}. The HOMO and LUMO positions and the bandgaps were determined from the extrapolation of the DOS band tails plotted on a linear scale, as shown in Figure S3 (Supporting Information). The data are summarized in Table S1 (Supporting Information). The measured DOS spectra (Figure 4a) indicate a gradual widening of the bandgap with increasing annealing time from 4 to 6s. It is evident that between 3 and 4 s, when rapid crystallization of the precursor proceeds toward the perovskite phase, the bandgap is narrowed due to a shift of the LUMO. Over the next 2 s, the bandgap of the perovskite layer is gradually widened due to a shift of the HOMO, while the LUMO is at the same position within the experimental error.

Moreover, the DOS spectra in the bandgap reveal a decreasing density of the trap states with increasing annealing time. The integral density of the trap states (DOS integral between HOMO and LUMO) is depicted in Figure 4b. This suggests that the formation of a continuous perovskite layer composed of uniaxially oriented grains leads to a marked decrease of the trap-state density in the bandgap. We prepared a perovskite film from the same precursor solution to validate this assumption, but without the MACl additive, using the conventional antisolvent method. Such a film had a random orientation of the perovskite grains, as verified by GIWAXS. In Figure S4 (Supporting Information), the measured DOS of the perovskite layer prepared by the antisolvent method is compared to that of FIRA with 10% MACl. In fact, the film prepared by 6 s FIRA processing has a trap-state density about an order of magnitude lower than the film prepared by the antisolvent method. Assuming that a low trap-state density reduces the electron/hole recombination rate in PSCs, this fact has significant implications for maximizing the short-circuit current density of PSCs manufactured by FIRA.[15]

In the following text, we will focus on the relationship between the mosaicity and DOS of the perovskite films prepared by FIRA. To examine these correlations, we performed in situ and real-time GIWAXS experiments during FIRA processing. The precursor solutions with the MACl molar fraction of 10% were spin-coated in a custom-designed FIRA chamber and GIWAXS patterns were continuously measured during the heating and cooling periods. In addition, we inspected the GIWAXS patterns before and after the FIRA application.

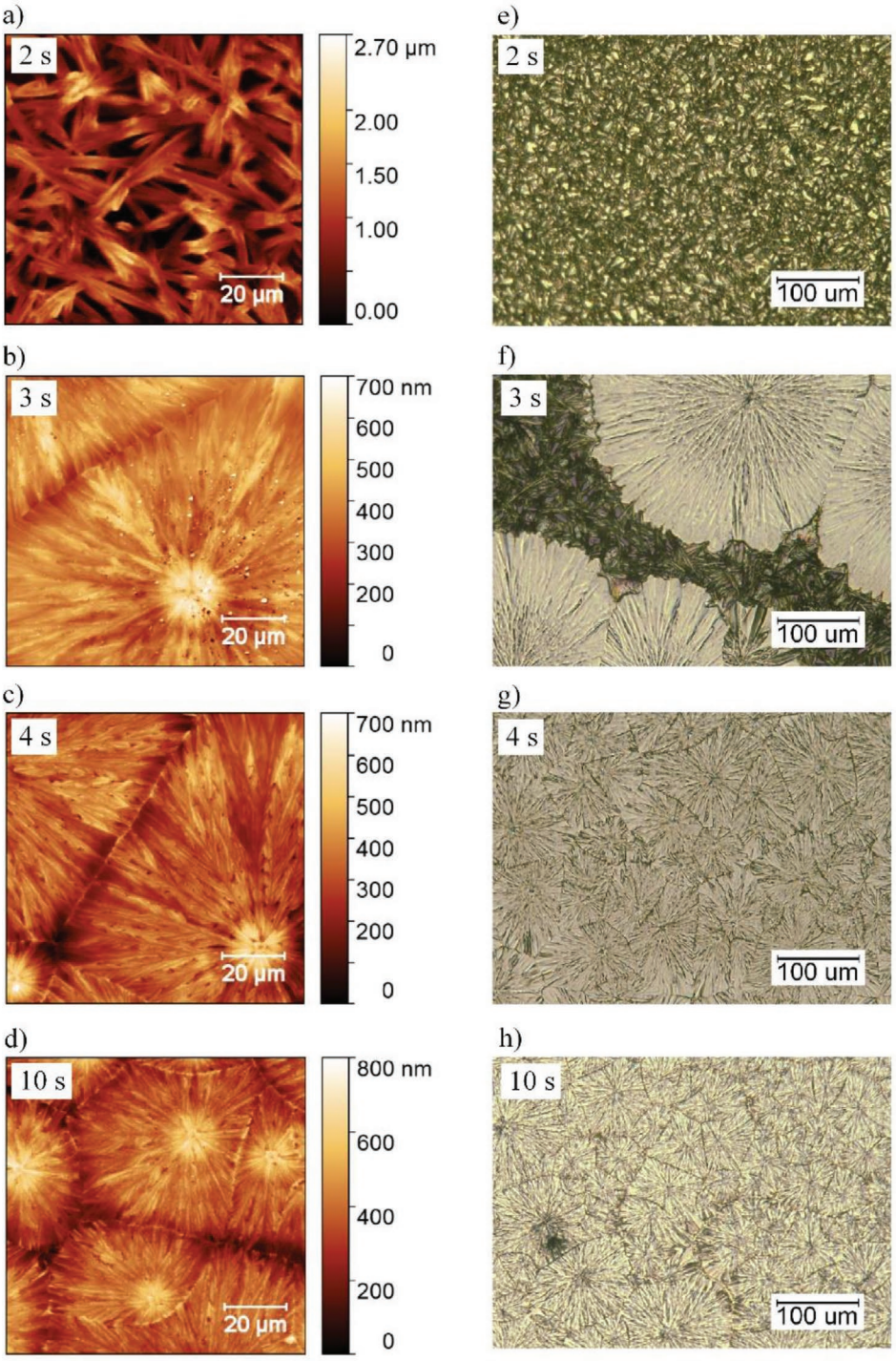

Figure 3. Influence of the annealing time on the perovskite film topography. a–d) AFM images (left) and e–h) optical microscopy (right) of the perovskite films annealed for different periods. The annealing times are indicated in the upper left corner.

The GIWAXS pattern recorded prior to the FIRA application shown in **Figure 5**a reveals a broad diffraction ring at $q \approx 0.5$ nm^{-1}, which is related to the scattering from intermediate adduct phases of precursor molecules in the liquid phase.[45,48] Figure 5b shows a GIWAXS pattern recorded after 5.5 s of FIRA. At this stage, the temperature of the film was above the phase transition temperature from the tetragonal to the cubic structure (≈55 °C). For this reason, the indexing of diffraction spots differs from those shown in Figure 1 for the perovskite films measured at room temperature. The diffraction pattern confirms a uniaxially oriented cubic structure of MAPI grains immediately after the conversion of the precursor

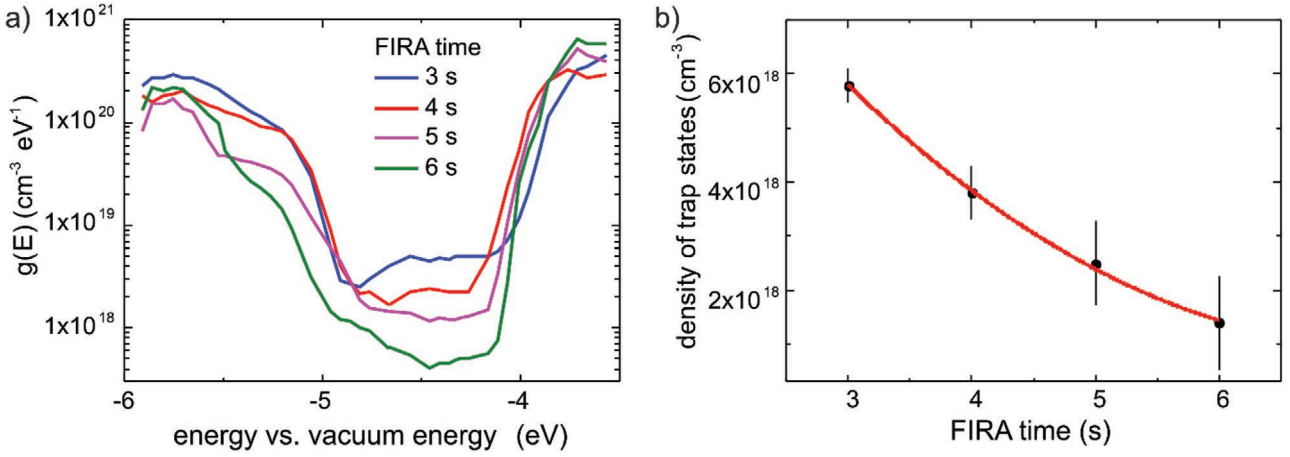

Figure 4. Ex situ ER-EIS spectroscopy. a) DOS spectra of the perovskite layers prepared by FIRA for different annealing times. b) The integral density of trap states between HOMO and LUMO calculated from the DOS spectra shown in (a). The red line is a guide to the eye.

into the perovskite layer and before the phase transition to the tetragonal structure. Assuming instantaneous perovskite conversion at the exact temperature of the phase transition and knowing the coefficient of thermal expansion of the MAPI crystal lattice, we can accurately track the point of perovskite conversion and temperature evolution. A detailed discussion on the phase transformation from the cubic to the tetragonal phase in the cool-down period, supplemented by the evaluation of the perovskite conversion temperature, can be found in the Supporting Information.

To better understand the transformation of the wet precursor film into a solid perovskite layer under FIRA, we plotted radially integrated q cuts shortly before and during FIRA processing. To obtain X-ray scattering profiles independent of possible changes in the mosaicity of the MAPI layers, the q cuts shown in **Figure 6**a were integrated using χ values in the interval from −90° to 90° ($\chi = 0°$ for $q_r = 0$). The broad peak at $q \approx 0.5$ nm^{-1} assigned to the precursor phase and the simultaneous appearance of the 001 perovskite diffraction peak at $q \approx 1$ nm^{-1} confirm that the conversion to the perovskite phase started ≈2.7 s after starting FIRA. No further significant changes in the scattering profiles were observed after 5 s of FIRA.

As already concluded from Figure 1, the final perovskite films exhibit a uniaxial texture with the (112) lattice planes parallel to the sample surface. To follow the possible changes in mosaicity during FIRA processing, we plotted the diffracted intensity from (001) planes as a function of the azimuthal χ angle in Figure 6b. These χ profiles correspond to the azimuthal cross-sections of 001 pole figures. The χ profiles confirm a low mosaicity from the very beginning manifested by the 001 diffraction peak developing at a χ value of 45.2° with the width (FWHM) of only 3.1°. No significant changes in either the maximum peak position or the peak width were observed during FIRA processing (Figure S10, Supporting Information). These results confirm that the preferential orientation of the perovskite layer is maintained throughout the FIRA process.

In the following text, we will inspect the temporal evolution of the principal diffraction peaks of the respective phases observed in GIWAXS patterns during FIRA. In particular, we assessed the intensities of the precursor and perovskite peaks. In addition, we followed the backconversion of perovskite to PbI_2. To determine the intensities, we used numerical trapezoidal integration in the selected areas of GIWAXS reciprocal space maps. The intensity of the precursor peak was determined

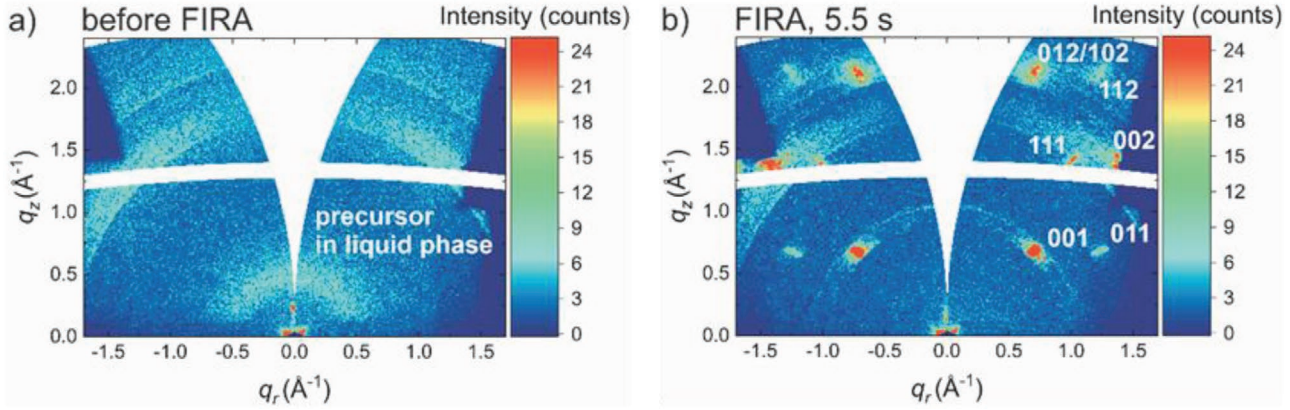

Figure 5. The GIWAXS patterns of MACl:MAI (10%) perovskite layer a) before and b) after 5.5 s application of FIRA.

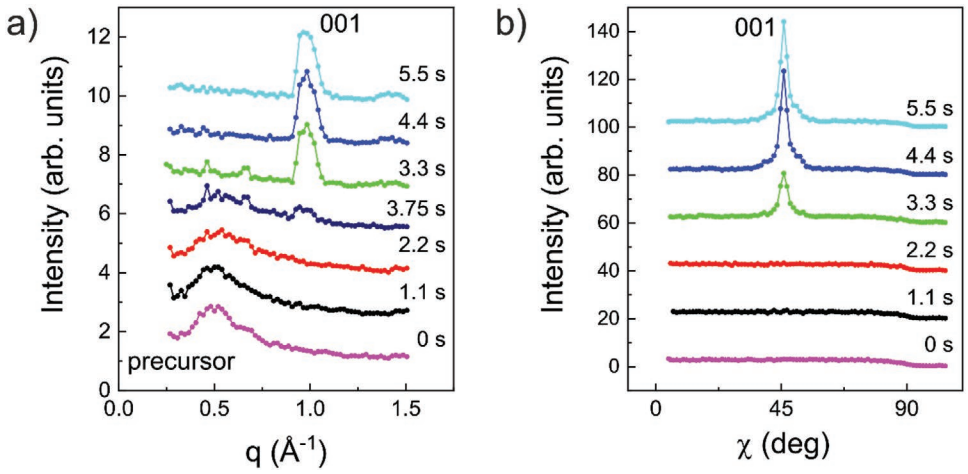

Figure 6. Time-resolved GIWAXS during FIRA. a) The evolution of the scattering profiles as a function of the FIRA time. b) The azimuthal χ distribution of 001 diffraction as a function of the FIRA time. The q values were integrated in the range 0.92–1.1 Å^{-1}.

by the integration between the q values 0.25 and 0.8 Å^{-1} and χ values −90° and 90°. The intensity of the 001 perovskite peak was integrated between the q values 0.93 and 1.06 Å^{-1} and χ values 26° and 66°. Finally, the PbI_2 001 peak was integrated between the q values 0.83 and 0.93 Å^{-1} and the χ values −25° and 25°. The integral intensities of these peaks are shown in **Figure 7** as a function of FIRA time. Furthermore, selected data from Figures 3 and 4 for the respective FIRA times are insetted in Figure 7 to correlate the perovskite conversion data with surface topography and trap-state density.

The zero time refers to the activation of the FIRA process, which lasted 10 s in total. After this time, the FIRA chamber cooled down spontaneously. In the first 3 s after switching on the FIRA process, we observed only the scattering signal

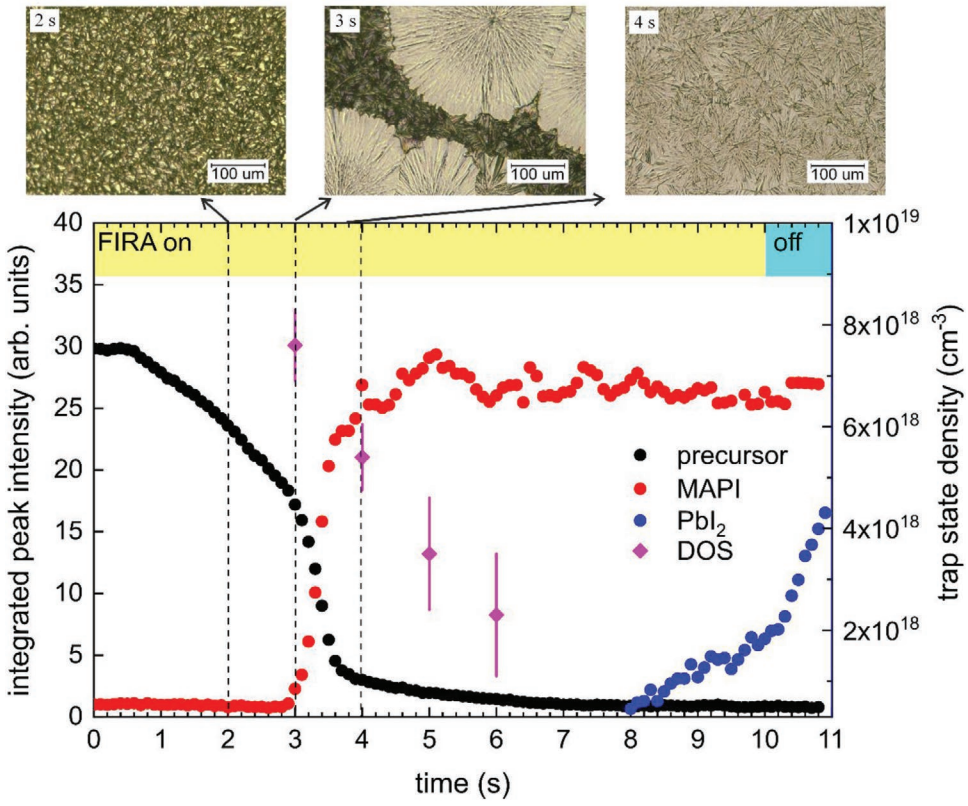

Figure 7. The correlation between the perovskite conversion, surface topography, and trap-state density during the FIRA process. The integral intensities were scaled to the same range to allow easy assessment of the identification of the perovskite transformation process. The scale bar in the microscopy images is 100 µm.

from the precursor phase, which decreased over time. At this stage, the spin-coated film was still in a wet state. Microscopic images confirmed a delayed crystallization after the sample was removed from the FIRA chamber. The resulting films were discontinuous and not suitable for solar cell production. Rapid crystallization of the perovskite film started after the first 3 s of FIRA processing. This was observed using GIWAXS and also directly in the FIRA chamber as a rapid change in film color from yellow to black. Microscopic images also showed some well-developed crystalline areas. The samples removed at this stage for the ex situ measurements were still partially wet. The measured density of trap states was around 6×10^{18} cm^{-3} after 3 s of FIRA and dropped rapidly after 4 s. Here, the samples exhibited continuous perovskite films, but GIWAXS revealed still not fully converted perovskite structures. Consistent with this, the conversion of precursor into perovskite structure was still in progress after the first 4 s, but at a much slower rate compared to the period between 3 and 4 s. The trap-state density decreased proportionally with increasing the annealing time and reached a value close to 1.5×10^{18} cm^{-3} for 6 s of FIRA processing time. A further increase of the annealing time beyond 8 s was associated with the conversion of the perovskite phase back into PbI_2 precursor. This conversion continued even after the FIRA was switched off, presumably due to the still favorable conditions for the perovskite decomposition. Hence, our time-resolved study clearly identified the narrow temporal FIRA window necessary for rapid thermal annealing of perovskite films for photovoltaic applications. Under our experimental conditions, the narrow processing window opens between 6 and 8 s. Here, the perovskite layers exhibited the highest crystallinity and the lowest trap-state density.

3. Conclusion

Fast and reliable preparation of perovskite films on flexible substrates suitable for roll-to-roll technology is essential for the successful launch of the next generation of solar cells. Our study focused on the recently introduced FIRA technology for rapid annealing of perovskite films on a timescale of a few seconds. First, we investigated the influence of MACl additive on the crystal structure of perovskite films. We found that a 10% molar fraction of MACl induced the lowest mosaicity of the film with the (112) lattice planes parallel to the substrate. The surface topography of such prepared layers is continuous without any pinholes, as confirmed by visible and atomic force microscopies. In addition, ex situ ER-EIS measurements confirmed an order of magnitude lower trap-state density compared to the layers prepared by the antisolvent technique. Finally, employing the time-resolved GIWAXS technique, we identified the best processing window for the annealing time of perovskite layers while using FIRA. Therefore, our study has direct implications for optimizing the FIRA technology of MAPI-based perovskite films using the MACl additive and roll-to-roll large-scale manufacturing of the next generation of perovskite solar cells. Most importantly, we have shown that the combination of time-resolved GIWAXS and ER-EIS allows identifying the correct time windows for rapidly evolving crystallization processes in general.

4. Experimental Section

Materials and Preparation of Perovskite Layers: DMF and dimethyl sulfoxide (DMSO) were purchased from Sigma-Aldrich, lead(II) iodide from TCI, MAI from Dyenamo, methylammonium chloride (MACl) from Borun New Materials, and poly(3,4-ethylenedioxythiophene):poly(styrene sulfonate) (PEDOT:PSS) from Ossila. The solvents were dehydrated with molecular sieves. The other chemicals were used as delivered.

The indium tin oxide (ITO)-coated glasses (surface resistivity 7 Ω sq^{-1}) were sonicated in acetone and isopropanol for 10 min. Cleaned substrates were then treated by UV–ozone. PEDOT:PSS was sonicated for 30 min, filtered using polyvinylidene fluoride (PVDF) filter with 0.45 µm pores, spin-coated on ITO substrates at 5000 rpm for 45 s, and subsequently annealed on a hot plate at 120 °C.

MAPI perovskite solutions were mixed in a nitrogen-filled glove box. For the standard solution, 652.5 mg of PbI_2 and 225.1 mg of MAI were diluted in a solvent mixture consisting of 900 µL DMF and 100 µL DMSO. When preparing the solutions with an additive, the 5, 10, 20, 30, 40, and 50% molar fractions of MAI were replaced by MACl. All perovskite solutions were stirred overnight. Before use, the perovskite solutions were filtered through a polytetrafluoroethylene filter with 0.45 µm pores, then spin-coated on ITO/PEDOT:PSS substrate at 2000 rpm for 10 s and annealed by FIRA.

The In Situ and Ex Situ GIWAXS: A table-top custom-designed laboratory GIWAXS system was employed for ex situ studies of the FIRA perovskite crystallization. The GIWAXS system utilized a microfocus X-ray source equipped with focusing Montel optics (IµS, Incoatec, Germany). The X-ray energy was 8.04 keV (Cu Kα radiation). The X-ray beam at the exit of the Montel optics had a total photon flux of 3×10^8 photons s^{-1} and a divergence of 5 mrad, the focal spot size being 400 µm (FWHM). To remove the primary (nonreflected) beam and single reflected beams from the Montel optics, a scatterless Ge pinhole with a diameter of 3 mm was used. The final photon flux behind the scatterless pinhole was 10^8 photons s^{-1}. The sample was placed in the focus of the Montel optics to maximize the diffraction signal from the perovskite film. The GIWAXS patterns were recorded by a 2D X-ray detector (Pilatus 200K, Dectris, Switzerland) placed at a distance of 8.6 cm from the sample center. The angle of incidence was set to 1.8°. The GIWAXS patterns were converted into q-space coordinates (q_r, q_z), where the q_r and q_z described the wavevector transfer components parallel and perpendicular to the sample surface, respectively.

The real-time and in situ GIWAXS crystallization experiments during FIRA were performed at the P03 beamline, PETRA III synchrotron radiation facility (DESY, Hamburg, Germany)[67] using a photon energy of 11.4 keV. The angle of incidence on the sample surface was set to 0.5°. The sample holder was located in an aluminum heating chamber equipped with two 600 W infrared halogen lamps (model 09751713, Heraeus Noblelight, Germany). The details of the temperature evolution during the annealing period can be found in the Supporting Information. The heating chamber was mounted on a hexapod motion platform (H-811, Physik Instrumente, Germany). The scattered X-ray photons were detected by a 2D detector (Pilatus 300K, Dectris, Switzerland). The exposure time was set to 20 ms, and an additional time of 5 ms was required for the image processing, which means that the time between consecutive images was set to 25 ms. The total measurement consisted of 2000 images, meaning that a single experiment lasted 50 s. A transistor–transistor logic (TTL) electronic signal from the X-ray detector was used to trigger the FIRA, which was switched on after 10 s of acquisition and continued for another 10 s. After switching off the FIRA, the changes in the perovskite layer were monitored for another 30 s. The implementation of the FIRA chamber on the beamline is shown in Figure S1 (Supporting Information).

Measurement of Surface Topography: AFM and optical microscopy were used to study the surface topography of FIRA-annealed perovskite films. To obtain surface images on the nanoscale, an AFM device (Dimension Edge, Bruker, USA) working in the tapping mode was used. The digital optical microscope (VHX-500, Keyence, USA) operating in the reflected light was employed to observe the surface topography on the microscale.

ER-EIS: The ER-EIS measures the DOS between HOMO and LUMO bands. It is based on the interaction between the perovskite film and electrolyte via reduction–oxidation reactions. In ER-EIS experiments, the electrochemical cells were attached to conductive ITO substrates covered with 40 nm thick PEDOT:PSS layers and FIRA-annealed perovskite layers, which formed working electrodes. Details of measuring principles and evaluation can be found in the Supporting Information.

Supporting Information

Supporting Information is available from the Wiley Online Library or from the author.

Acknowledgements

The authors acknowledge the financial support of the project Grant Nos. SK-CN-RD-18-0006, APVV-17-0352, APVV-15-0641, APVV-15-0693, APVV-18-0480, APVV-19-0465, APVV-19-0365, APVV-14-074, VEGA 2/0041/21, 2/0149/17, VEGA 2/0129/19, VEGA 2/0081/18, ITMS 26230120002, ITMS 26210120002, National Key Research and Development Program of China (2017YFE0119700), DAAD/SAV and the funding by the DFG. This work was performed during the implementation of the project Building-up Centre for Advanced Materials Application of the Slovak Academy of Sciences, ITMS Project Code 313021T081 supported by the Integrated Infrastructure Operational Programme funded by the ERDF.

Conflict of Interest

The authors declare no conflict of interest.

Data Availability Statement

Research data are not shared.

Keywords

impedance spectroscopy, infrared annealing, perovskites, solar cells, X-ray scattering

Received: March 4, 2021
Revised: May 6, 2021
Published online: June 26, 2021

[1] A. Kojima, K. Teshima, Y. Shirai, T. Miyasaka, *J. Am. Chem. Soc.* **2009**, *131*, 6050.
[2] M. M. Lee, J. Teuscher, T. Miyasaka, T. N. Murakami, H. J. Snaith, *Science* **2012**, *338*, 643.
[3] M. Xiao, F. Huang, W. Huang, Y. Dkhissi, Y. Zhu, J. Etheridge, A. Gray-Weale, U. Bach, Y.-B. B. Cheng, L. Spiccia, *Angew. Chem.* **2014**, *53*, 9898.
[4] N. J. Jeon, J. H. Noh, Y. C. Kim, W. S. Yang, S. Ryu, S. Il Seok, *Nat. Mater.* **2014**, *13*, 897.
[5] R. Swartwout, M. T. Hoerantner, V. Bulović, *Energy Environ. Mater.* **2019**, *2*, 119.
[6] F. Huang, M. Li, P. Siffalovic, G. Cao, J. Tian, *Energy Environ. Sci.* **2019**, *12*, 518.
[7] K. Yan, M. Long, T. Zhang, Z. Wei, H. Chen, S. Yang, J. Xu, *J. Am. Chem. Soc.* **2015**, *137*, 4460.
[8] P. Docampo, F. C. Hanusch, S. D. Stranks, M. Döblinger, J. M. Feckl, M. Ehrensperger, N. K. Minar, M. B. Johnston, H. J. Snaith, T. Bein, *Adv. Energy Mater.* **2014**, *4*, 1400355.
[9] B. Li, M. Li, C. Fei, G. Cao, J. Tian, *J. Mater. Chem. A* **2017**, *5*, 24168.
[10] D. P. Nenon, J. A. Christians, L. M. Wheeler, J. L. Blackburn, E. M. Sanehira, B. Dou, M. L. Olsen, K. Zhu, J. J. Berry, J. M. Luther, *Energy Environ. Sci.* **2016**, *9*, 2072.
[11] M. Wang, B. Li, P. Siffalovic, L.-C. Chen, G. Cao, J. Tian, *J. Mater. Chem. A* **2018**, *6*, 15386.
[12] K. Odysseas Kosmatos, L. Theofylaktos, E. Giannakaki, D. Deligiannis, M. Konstantakou, T. Stergiopoulos, *Energy Environ. Mater.* **2019**, *2*, 79.
[13] S. Sánchez, X. Hua, A. Günzler, E. Bermúdez-Ureña, D. Septiadi, M. Saliba, U. Steiner, *Cryst. Growth Des.* **2020**, *20*, 670.
[14] S. Sanchez, U. Steiner, X. Hua, *Chem. Mater.* **2019**, *31*, 3498.
[15] S. Sánchez, M. Vallés-Pelarda, J.-A. A. Alberola-Borràs, R. Vidal, J. J. Jerónimo-Rendón, M. Saliba, P. P. Boix, I. Mora-Seró, *Mater. Today* **2019**, *31*, 39.
[16] S. Sánchez, J. Jerónimo-Rendon, M. Saliba, A. Hagfeldt, *Mater. Today* **2020**, *35*, 9.
[17] S. Sanchez, N. Christoph, B. Grobety, N. Phung, U. Steiner, M. Saliba, A. Abate, *Adv. Energy Mater.* **2018**, *8*, 1802060.
[18] S. Sanchez, X. Hua, N. Phung, U. Steiner, A. Abate, *Adv. Energy Mater.* **2018**, *8*, 1702915.
[19] Z. Chen, B. Turedi, A. Y. Alsalloum, C. Yang, X. Zheng, I. Gereige, A. Alsaggaf, O. F. Mohammed, O. M. Bakr, *ACS Energy Lett.* **2019**, *4*, 1258.
[20] N. Giesbrecht, J. Schlipf, I. Grill, P. Rieder, V. Dyakonov, T. Bein, A. Hartschuh, P. Müller-Buschbaum, P. Docampo, *J. Mater. Chem. A* **2018**, *6*, 4822.
[21] W. Shockley, H. J. Queisser, *J. Appl. Phys.* **1961**, *32*, 510.
[22] T. Kirchartz, U. Rau, *Adv. Energy Mater.* **2018**, *8*, 1703385.
[23] L. A. Muscarella, E. M. Hutter, S. Sanchez, C. D. Dieleman, T. J. Savenije, A. Hagfeldt, M. Saliba, B. Ehrler, *J. Phys. Chem. Lett.* **2019**, *10*, 6010.
[24] D. W. Dequilettes, K. Frohna, D. Emin, T. Kirchartz, V. Bulovic, D. S. Ginger, S. D. Stranks, *Chem. Rev.* **2019**, *119*, 11007.
[25] C. M. Wolff, P. Caprioglio, M. Stolterfoht, D. Neher, *Adv. Mater.* **2019**, *31*, 1902762.
[26] S. D. Stranks, *ACS Energy Lett.* **2017**, *2*, 1515.
[27] M. Abdi-Jalebi, Z. Andaji-Garmaroudi, S. Cacovich, C. Stavrakas, B. Philippe, J. M. Richter, M. Alsari, E. P. Booker, E. M. Hutter, A. J. Pearson, S. Lilliu, T. J. Savenije, H. Rensmo, G. Divitini, C. Ducati, R. H. Friend, S. D. Stranks, *Nature* **2018**, *555*, 497.
[28] I. L. Braly, D. W. Dequilettes, L. M. Pazos-Outón, S. Burke, M. E. Ziffer, D. S. Ginger, H. W. Hillhouse, *Nat. Photonics* **2018**, *12*, 355.
[29] Y. Hu, E. M. Hutter, P. Rieder, I. Grill, J. Hanisch, M. F. Aygüler, A. G. Hufnagel, M. Handloser, T. Bein, A. Hartschuh, K. Tvingstedt, V. Dyakonov, A. Baumann, T. J. Savenije, M. L. Petrus, P. Docampo, *Adv. Energy Mater.* **2018**, *8*, 1703057.
[30] I. Levine, O. G. Vera, M. Kulbak, D. R. Ceratti, C. Rehermann, J. A. Márquez, S. Levcenko, T. Unold, G. Hodes, I. Balberg, D. Cahen, T. Dittrich, *ACS Energy Lett.* **2019**, *4*, 1150.
[31] A. F. Castro-Méndez, J. Hidalgo, J. P. Correa-Baena, *Adv. Energy Mater.* **2019**, *9*, 1901489.
[32] Z. Ni, C. Bao, Y. Liu, Q. Jiang, W. Q. Wu, S. Chen, X. Dai, B. Chen, B. Hartweg, Z. Yu, Z. Holman, J. Huang, *Science* **2020**, *367*, 1352.
[33] T. A. S. Doherty, A. J. Winchester, S. Macpherson, D. N. Johnstone, V. Pareek, E. M. Tennyson, S. Kosar, F. U. Kosasih, M. Anaya, M. Abdi-Jalebi, Z. Andaji-Garmaroudi, E. L. Wong, J. Madéo, Y. H. Chiang, J. S. Park, Y. K. Jung, C. E. Petoukhoff, G. Divitini, M. K. L. Man, C. Ducati, A. Walsh, P. A. Midgley, K. M. Dani, S. D. Stranks, *Nature* **2020**, *580*, 360.

[34] R. Wang, J. Xue, K. L. Wang, Z. K. Wang, Y. Luo, D. Fenning, G. Xu, S. Nuryyeva, T. Huang, Y. Zhao, J. L. Yang, J. Zhu, M. Wang, S. Tan, I. Yavuz, K. N. Houk, Y. Yang, *Science* **2019**, *366*, 1509.
[35] K. X. Steirer, P. Schulz, G. Teeter, V. Stevanovic, M. Yang, K. Zhu, J. J. Berry, *ACS Energy Lett.* **2016**, *1*, 360.
[36] M. Yavari, F. Ebadi, S. Meloni, Z. S. Wang, T. C.-J. Yang, S. Sun, H. Schwartz, Z. Wang, B. Niesen, J. Durantini, P. Rieder, K. Tvingstedt, T. Buonassisi, W. C. H. Choy, A. Filippetti, T. Dittrich, S. Olthof, J. P. Correa-Baena, W. Tress, *J. Mater. Chem. A* **2019**, *7*, 23838.
[37] X. Wu, M. T. Trinh, D. Niesner, H. Zhu, Z. Norman, J. S. Owen, O. Yaffe, B. J. Kudisch, X. Y. Zhu, *J. Am. Chem. Soc.* **2015**, *137*, 2089.
[38] J. Schlipf, P. Müller-Buschbaum, *Adv. Energy Mater.* **2017**, *7*, 1700131.
[39] K. Meng, X. Wang, Q. Xu, Z. Li, Z. Liu, L. Wu, Y. Hu, N. Liu, G. Chen, *Adv. Funct. Mater.* **2019**, *29*, 1902319.
[40] K. Wang, M. C. Tang, H. X. Dang, R. Munir, D. Barrit, M. De Bastiani, E. Aydin, D. M. Smilgies, S. De Wolf, A. Amassian, *Adv. Mater.* **2019**, *31*, 1808357.
[41] M. Qin, K. Tse, T. K. Lau, Y. Li, C. J. Su, G. Yang, J. Chen, J. Zhu, U. S. Jeng, G. Li, H. Chen, X. Lu, *Adv. Mater.* **2019**, *31*, 1901284.
[42] Y. Zhong, R. Munir, J. Li, M.-C. Tang, M. R. Niazi, D.-M. Smilgies, K. Zhao, A. Amassian, *ACS Energy Lett.* **2018**, *3*, 1078.
[43] K. Bruening, B. Dou, J. Simonaitis, Y. Y. Lin, M. F. A. M. van Hest, C. J. Tassone, *Joule* **2018**, *2*, 2464.
[44] J. Li, R. Munir, Y. Fan, T. Niu, Y. Liu, Y. Zhong, Z. Yang, Y. Tian, B. Liu, J. Sun, D.-M. Smilgies, S. Thoroddsen, A. Amassian, K. Zhao, S. (Frank) Liu, *Joule* **2018**, *2*, 1313.
[45] K. Meng, L. Wu, Z. Liu, X. Wang, Q. Xu, Y. Hu, S. He, X. Li, T. Li, G. Chen, *Adv. Mater.* **2018**, *30*, 1706401.
[46] M. Alsari, O. Bikondoa, J. Bishop, M. Abdi-Jalebi, L. Y. Ozer, M. Hampton, P. Thompson, M. T. Hörantner, S. Mahesh, C. Greenland, J. E. Macdonald, G. Palmisano, H. J. Snaith, D. G. Lidzey, S. D. Stranks, R. H. Friend, S. Lilliu, *Energy Environ. Sci.* **2018**, *11*, 383.
[47] S. Lilliu, J. Griffin, A. T. Barrows, M. Alsari, B. Curzadd, T. G. Dane, O. Bikondoa, J. E. Macdonald, D. G. Lidzey, *CrystEngComm* **2016**, *18*, 5448.
[48] A. T. Barrows, S. Lilliu, A. J. Pearson, D. Babonneau, A. D. F. Dunbar, D. G. Lidzey, *Adv. Funct. Mater.* **2016**, *26*, 4934.
[49] Y. Yang, S. Feng, M. Li, W. Xu, G. Yin, Z. Wang, B. Sun, X. Gao, *Sci. Rep.* **2017**, *7*, 46724.
[50] D. T. Moore, H. Sai, K. W. Tan, D. M. Smilgies, W. Zhang, H. J. Snaith, U. Wiesner, L. A. Estroff, *J. Am. Chem. Soc.* **2015**, *137*, 2350.
[51] R. Munir, A. D. Sheikh, M. Abdelsamie, H. Hu, L. Yu, K. Zhao, T. Kim, O. El Tall, R. Li, D. M. Smilgies, A. Amassian, *Adv. Mater.* **2017**, *29*, 1604113.
[52] T. Miyadera, Y. Shibata, T. Koganezawa, T. N. Murakami, T. Sugita, N. Tanigaki, M. Chikamatsu, *Nano Lett.* **2015**, *15*, 5630.
[53] C. Y. Chang, Y. C. Huang, C. S. Tsao, W. F. Su, *ACS Appl. Mater. Interfaces* **2016**, *8*, 26712.
[54] Y. C. Huang, C. S. Tsao, Y. J. Cho, K. C. Chen, K. M. Chiang, S. Y. Hsiao, C. W. Chen, C. J. Su, U. S. Jeng, H. W. Lin, *Sci. Rep.* **2015**, *5*, 13657.
[55] M. Abdelsamie, J. Xu, K. Bruening, C. J. Tassone, H.-G. Steinrück, M. F. Toney, *Adv. Funct. Mater.* **2020**, *30*, 2001752.
[56] J. Ogle, D. Powell, E. Amerling, D. M. Smilgies, L. Whittaker-Brooks, *CrystEngComm* **2019**, *21*, 5707.
[57] A. Greco, A. Hinderhofer, M. I. Dar, N. Arora, J. Hagenlocher, A. Chumakov, M. Grätzel, F. Schreiber, *J. Phys. Chem. Lett.* **2018**, *9*, 6750.
[58] F. Staub, U. Rau, T. Kirchartz, *ACS Omega* **2018**, *3*, 8009.
[59] J. M. Ball, A. Petrozza, *Nat. Energy* **2016**, *1*, 16149.
[60] V. Nádazdy, F. Schauer, K. Gmucová, *Appl. Phys. Lett.* **2014**, *105*, 142109.
[61] F. Schauer, L. Tkáč, M. Ožvoldová, V. Nádaždy, K. Gmucová, M. Jergel, P. Šiffalovič, *AIP Adv.* **2017**, *7*, 055002.
[62] V. Nádaždy, K. Gmucová, P. Nádaždy, P. Siffalovic, K. Vegso, M. Jergel, F. Schauer, E. Majkova, *J. Phys. Chem. C* **2018**, *122*, 5881.
[63] S. Athanasopoulos, F. Schauer, V. Nádaždy, M. Weiß, F. J. Kahle, U. Scherf, H. Bässler, A. Köhler, *Adv. Energy Mater.* **2019**, *9*, 1900814.
[64] T. J. Jacobsson, L. J. Schwan, M. Ottosson, A. Hagfeldt, T. Edvinsson, *Inorg. Chem.* **2015**, *54*, 10678.
[65] P. Nandi, C. Giri, B. Joseph, S. Rath, U. Manju, D. Topwal, *J. Phys. Chem. A* **2016**, *120*, 9732.
[66] F. Schauer, V. Nádady, K. Gmucová, T. Váry, *J. Appl. Phys.* **2018**, *124*, 165702.
[67] A. Buffet, A. Rothkirch, R. Döhrmann, V. Körstgens, M. M. Abul Kashem, J. Perlich, G. Herzog, M. Schwartzkopf, R. Gehrke, P. Müller-Buschbaum, S. V. Roth, *J. Synchrotron Radiat.* **2012**, *19*, 647.